WILEY | Hindawi

Research Article

Experimental Study of Hysteresis Characteristics of Water-Sediment Mixture Seepage in Rock Fractures

Lili Cao,[1] Pu Zhang [ID],[1] Jiazhi Zhang,[2] Gang Lin,[2] Izhar Mithal Jiskani [ID],[3] Zhanqing Chen,[2] Zhifei Wang,[2] and Ming Li[2]

[1]*School of Medical Information and Engineering, Xuzhou Medical University, Xuzhou, 221004 Jiangsu, China*
[2]*State Key Laboratory for Geomechanics and Deep Underground Engineering, China University of Mining and Technology, Xuzhou, 221116 Jiangsu, China*
[3]*School of Mines, China University of Mining and Technology, Xuzhou, 221116 Jiangsu, China*

Correspondence should be addressed to Pu Zhang; zptulun@163.com

The hysteresis of water-sediment mixture seepage in rock fractures is one of the critical factors which affect the determination of the timing of coal mine water inrush disasters prevention and control. In this paper, a mechanical model was established to study the hysteresis whose criteria were also put forward. The area of the hysteresis loop and the maximum pressure gradient were selected as characterization parameters of hysteresis. On this basis, an experimental system was established to study influences of different sand particle size, sand mass concentration, and fracture opening on water-sediment mixture seepage in rock fractures. The results indicated that the increase in the sand particle size and sand mass concentration could effectively enhance hysteresis characteristics of specimen fractures. While hysteresis characteristics decreased significantly with the increase of fracture opening. The research results are useful to prevent and control water inrush disasters of coal mine.

1. Introduction

Water inrush accidents are one of the serious coal mine disasters, which pose threats to production safety in China. A large number of casualties because of water inrush accidents occur every year, with incalculable economic losses [1]. It is a mining-induced hazard. Damages occur around the surrounding rock during the coal mining process. The accumulation of damages leads to macroscopic cracks inside the surrounding rock [2]. At this point, water and fine particulate matter in the strata will enter the mining space through fractured channels [3, 4]. A mine water inrush disaster is finally formed with a large water flow. Essentially, the mechanical mechanism of coal mining water inrush is rock mass instability triggered by the seepage of water-sediment mixture in rock fissures [5–7]. Meanwhile, the rock mass instability could accelerate inrushing amount. Therefore,

the key to prevent coal mine water inrush disasters is to get water-sediment mixture seepage characteristics in rock fissure.

Liquid seepage not only exits inside rock fissures during the coal mining process, but also could be found in geotechnical engineering such as tunnels, foundation pits, and slopes. Therefore, the research on seepage characteristics inside rock fissures is always a hotspot [8–10]. Scholars have studied the influences of surface roughness of fracture, loading conditions, and stress paths on seepage in rock fissures through laboratory tests [11–15]. Considering the relatively complex distribution and characteristics of natural fractures, the research of seepage characteristics inside the prefabricated cracks is hard to provide references for the actual engineering, while the numerical calculation could solve the dilemma [16, 17]. At the same time, the development and maturity of a series of mathematical algorithms and

theoretical models have also enriched seepage theories and provided theoretical support for water inrush disaster prevention and control [18–20]. Moreover, 3D printing technology has made it possible to accurately get initial fissures and their distribution characteristics inside the rock mass in recent years [21], leading to the seepage analysis of rock fractures moving from macroscopic domain towards microscopic and high-precision domain.

The transformation of research objects is key of solving water inrush problems. Liquid flow in the fracture was simplified approximately to water during the early stages by researchers, which greatly reduced the calculation difficulty. The results could reflect seepage law to a certain extent, but could not describe problems accurately. Then, scholars gradually took a water-sediment mixture as the object of study. Thus, the research of seepage in rock fractures gradually changes from the unidirectional flow into two-phase flow [22, 23]. Such transformation of research object increases the difficulty of experimental study and analysis complexity. Besides the fracture surface roughness, hydraulic pressure, etc., solution concentration and sand particle size also become variables of seepage characteristics [24]. Meanwhile, testing systems specially applied in flow-sediment mixture seepage are also key points of researches. In addition, the two-phase flow mechanical algorithm based on the basic mathematic model has also become an important theoretical tool for the research of water-sediment seepage characteristics [25, 26]. The popularization and application of business software for multifield coupling calculation and calculation software based on computer language also provide platforms for the research of seepage characteristics of water-sediment mixture in rock fractures under complex conditions [27, 28].

It could be found out that the research of water-sediment mixture seepage in rock fractures has transformed from macrocharacteristics to mesoscopic mechanism. The results indicate that water-sediment mixture seepage in rock fractures has remarkable hysteresis characteristics [29]. That is, the seepage pressure gradient and seepage velocity have obvious nonlinear variation characteristics, and the pressure gradient variation obviously lags behind that of seepage velocity. Hysteretic characteristics are common in geotechnical engineering [30–34]. The variation of slope stress usually lags behind that of slope deformation. There is lag time between the strongest scouring action of flood on the riverbed and the moment of flood peak. Therefore, it is of great significance for engineering safety protection to make clear the hysteresis. However, few studies have been carried out on hysteresis characteristics of water-sediment mixture seepage in rock fractures [35]. Such researches are necessary to accurately get signals of water inrush disasters and conduct disaster protection for coal mine. Under such background, a testing system will be designed to study hysteresis characteristics of water-sediment mixture seepage in rock fractures. The seepage mechanical model will be established in ideal rock mass fractures. On the basis, characterization parameters of hysteresis characteristics will be determined. The influences of sand particle size, sand mass concentration, and fracture opening on hysteresis characteristics will be analyzed in detail. The research results are aimed at providing references for the determination of the best time to prevent and control coal mine water inrush disasters [36].

2. The Experiment

2.1. Principle of the Experiment. A two-dimensional ideal mechanical model of seepage in rock fractures was established, as shown in Figure 1(a). In the model, the fluid flow direction is in the x-direction, y is the normal direction along the lower fissure surface, L is the size of the rock mass along x direction, b is the fracture opening, $v(y)$ is the seepage velocity distribution function of water-sediment mixture in the fracture, and $\vec{n}$ is the unit vector of the normal line of the lower fracture surface. Figure 1(b) shows the mechanics characteristics of the microsegment dx with the height of b in the x direction. τ_{yx}^{fs} is the resistance to the mixture from the fracture surface, P is seepage pressure, and V is the average seepage velocity.

According to the model in Figure 1, the following formula could be obtained:

$$V = \frac{1}{b} \int_0^b v(y) dy. \tag{1}$$

For the ideal rock fractures, the seepage velocity shows a parabolic distribution along the normal direction of the fracture surface, that is,

$$v(y) = \frac{4}{b^2} y(b-y) v_{\max}, \tag{2}$$

where $v_{\max}$ is the maximum flow velocity.

By substituting formula (2) into formula (1), the following formula could be obtained:

$$V = \frac{1}{b} \int_0^b \frac{4}{b^2} y(b-y) v_{\max} dy = \frac{2}{3} v_{\max}. \tag{3}$$

That is,

$$v_{\max} = \frac{3}{2} V. \tag{4}$$

By substituting formula (4) into formula (2), the following formula could be obtained:

$$v(y) = \frac{6}{b^2} y(b-y) V. \tag{5}$$

According to fluid mechanics, the shear stress τ_{yx}^{fs} on the fracture surface is related to the gradient of seepage velocity $\partial v / \partial y|_{y=0}$, that is,

$$\tau_{yx}^{fs} = C \left(\frac{\partial v}{\partial y}\bigg|_{y=0} \right)^k, \tag{6}$$
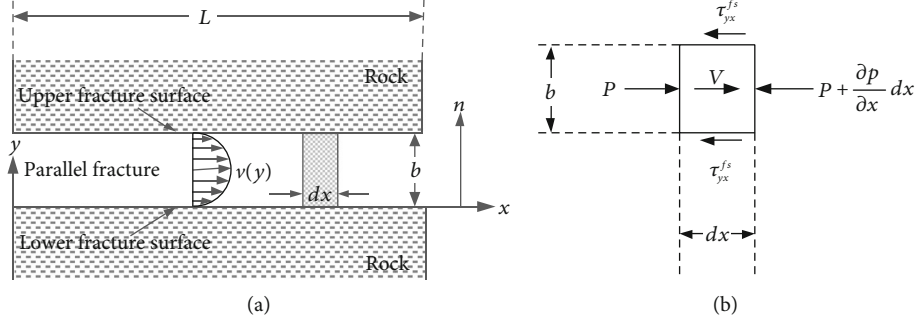
FIGURE 1: The two-dimensional ideal mechanical model of seepage in rock fractures: (a) model structure and mechanical characteristics and (b) mechanics characteristics of seepage liquid in dx.

where C is the consistency coefficient of the mixture, and k is the power exponent.

According to mechanics characteristics of the microliquid segment (Figure 1(b)), the equilibrium equation can be obtained as follows

$$\frac{\partial P}{\partial x} = -\frac{2}{b}\tau_{yx}^{fs}. \tag{7}$$

By substituting formulas (5) and (7) into formula (6), formula (8) could be obtained as follows

$$\frac{\partial P}{\partial x} = -\frac{2}{b}C\left(\frac{\partial v}{\partial y}\bigg|_{y=0}\right)^k = -\frac{2C}{b}\left(\frac{6}{b}V\right)^k. \tag{8}$$

Formula (8) is true when the distribution of seepage velocity is parabolic along the normal direction of the fissure surface. That is, if the average seepage velocities are the same during the loading and unloading process, the gradients of seepage velocities will be the same, that is,

$$V_{\mathrm{up}} = V_{\mathrm{down}} \Rightarrow \frac{\partial v}{\partial y}\bigg|_{y=0}^{\mathrm{up}} = \frac{\partial v}{\partial y}\bigg|_{y=0}^{\mathrm{down}}. \tag{9}$$

In fact, the seepage velocity of the mixture along the normal direction of the fracture surface is generally not in parabolic distribution. Even if the average seepage velocities are the same during the loading and unloading process, there will be differences between the gradients of the seepage velocities.

$$V_{\mathrm{up}} = V_{\mathrm{down}} \Rightarrow \frac{\partial v}{\partial y}\bigg|_{y=0}^{\mathrm{up}} \neq \frac{\partial v}{\partial y}\bigg|_{y=0}^{\mathrm{down}}. \tag{10}$$

Then, for formula (8), the following formula could be obtained:

$$G^{p\text{-}\mathrm{up}} = \frac{\partial P^{\mathrm{up}}}{\partial x} \neq G^{p\text{-}\mathrm{down}} = \frac{\partial P^{\mathrm{down}}}{\partial x}. \tag{11}$$

At the same time, if the following formula is true,

$$G^{p\text{-}\mathrm{up}} > G^{p\text{-}\mathrm{down}}\left(V_{\mathrm{up}} = V_{\mathrm{down}}\right), \tag{12}$$

hysteresis of mixture seepage could be found in rock fractures.

Therefore, an experiment was carried out to study hysteresis in water-sediment mixture seepage based on formulas (10)–(12). First, the seepage velocity was increased from V_1, V_2, $\cdots\cdots$ until V_n, and then decreased to V_1, V_2, $\cdots\cdots$ until V_n. The pressure gradients $G_1^{p\text{-}\mathrm{up}}$, $G_2^{p\text{-}\mathrm{up}}$,......, $G_n^{p\text{-}\mathrm{up}}$ and $G_1^{p\text{-}\mathrm{down}}$, $G_2^{p\text{-}\mathrm{down}}$,......, $G_n^{p\text{-}\mathrm{down}}$ were tested, respectively. Thus, the hysteresis characteristics in mixture seepage were studied by comparing values of $G_i^{p\text{-}\mathrm{up}}$ and $G_i^{p\text{-}\mathrm{down}}$.

2.2. Experimental Equipment and Specimen Preparations

2.2.1. Experimental Equipment. The independently designed test system for water-sediment seepage in rock fractures (TSWSPRF) was applied in the experiment. Figure 2 shows the system. It consists of a water-sediment mixture stirring system (I), water-sediment mixture transport system (II), control and data acquisition system (III), and fractured rock mass seepage system (IV). During the experiment, the mixture will be firstly stirred evenly to form a homogeneous solution. Then, the solution will be transported to the fractured rock mass seepage system through the transport system. Finally, the mixed solution will penetrate the fractures, and the seepage experiment will be completed.

During the experiment, the impeller (Figure 2 (5)) in the stirring system (Figure 2 I) drove the mixture rotation. The eddying effects could ensure a homogeneous mixture. After completing the stirring, the mixture was transported to the seepage system (Figure 2 IV) through the transport system (Figure 2 II). During the process, VVVF (Figure 2(d)) was used to adjust the single screw pump (Figure 2(c)) to provide power for the channel. The transportation pressure and flow of the water-sediment mixture were collected through a pressure transmitter (Figure 2(e)) and flow sensor (Figure 2(f)). The speed range of VVVF was between 0 and 1440 r/min. The maximum flow rate of the screw pump was 0.8 m3/h, and the range of the pressure sensor was between 0 and 21 MPa. The aforementioned parameters could meet the
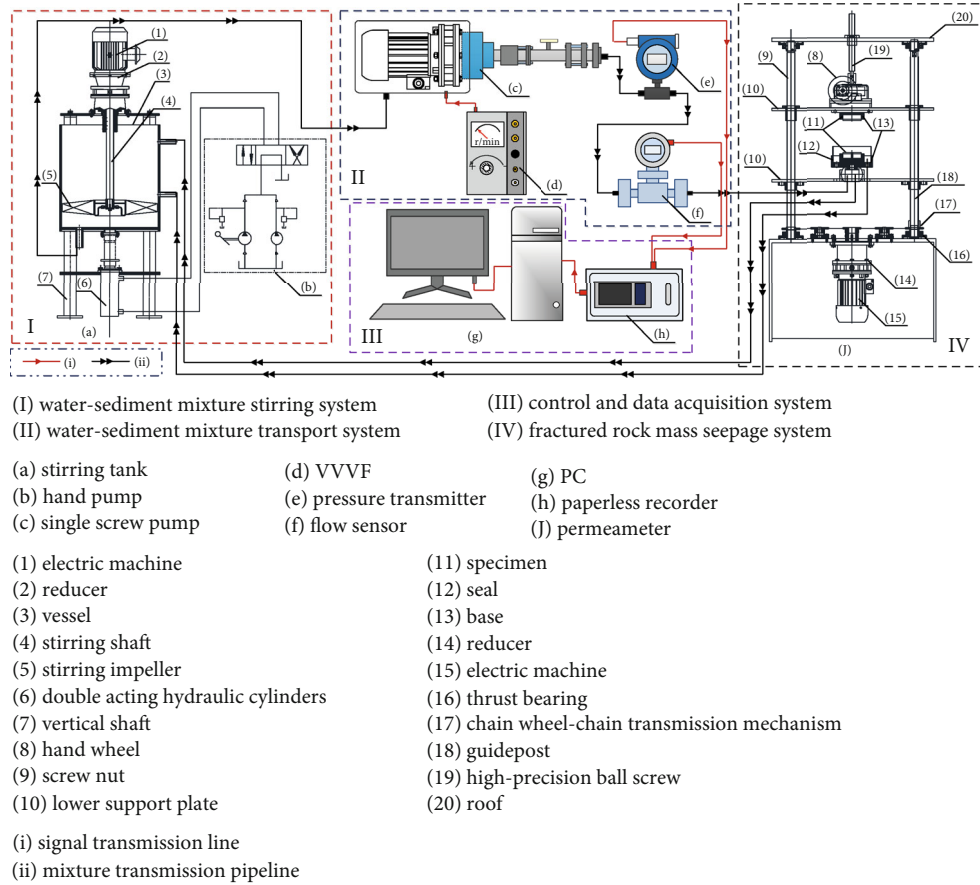
(I) water-sediment mixture stirring system
(II) water-sediment mixture transport system

(III) control and data acquisition system
(IV) fractured rock mass seepage system

(a) stirring tank
(b) hand pump
(c) single screw pump

(d) VVVF
(e) pressure transmitter
(f) flow sensor

(g) PC
(h) paperless recorder
(J) permeameter

(1) electric machine
(2) reducer
(3) vessel
(4) stirring shaft
(5) stirring impeller
(6) double acting hydraulic cylinders
(7) vertical shaft
(8) hand wheel
(9) screw nut
(10) lower support plate

(11) specimen
(12) seal
(13) base
(14) reducer
(15) electric machine
(16) thrust bearing
(17) chain wheel-chain transmission mechanism
(18) guidepost
(19) high-precision ball screw
(20) roof

(i) signal transmission line
(ii) mixture transmission pipeline

FIGURE 2: Testing system of water-sediment mixture seepage in rock fractures. (I) Water-sediment mixture stirring system. (II) Water-sediment mixture transport system. (III) Control and data acquisition system. (IV) Fractured rock mass seepage system. (a) stirring tank, (b) hand pump, (c) single screw pump, (d) VVVF, (e) pressure transmitter, (f) flow sensor, (g) PC, (h) paperless recorder, and (J) permeameter. (11) specimen, (12) seal, (1) electric machine, (2) reducer, (3) vessel, (4) stirring shaft, (5) stirring impeller, (6) double-acting hydraulic cylinders, (7) vertical shaft, (8) handwheel, (9) screw nut, (10) lower support plate, (13) base, (14) reducer, (15) electric machine, (16) thrust bearing, (17) chain wheel-chain transmission mechanism, (18) guidepost, (19) high-precision ball screw, and (20) roof. (i) Signal transmission line and (ii) mixture transmission pipeline.
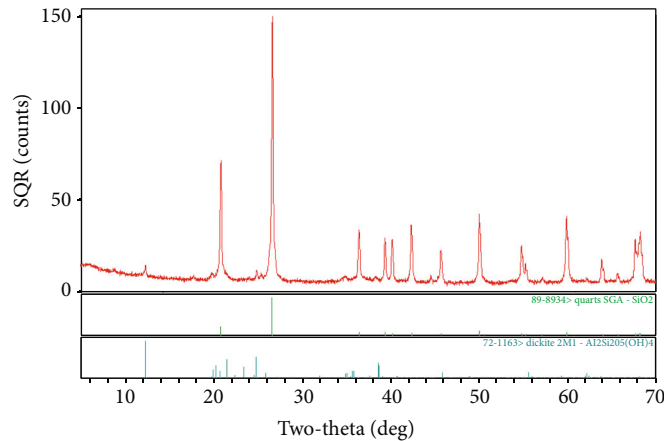

FIGURE 3: XRD test results of rock specimens compositions.

design requirements of this experiment. The seepage process was completed when the mixture was transported to the lower surface of the lower specimen and penetrated to frac-tures through round holes. The data were collected by sensors during the whole experiment and recorded by a paperless recorder (Figure 2(h)).

2.2.2. Specimen Preparations. As shown in Figure 3, the reddish-brown sandstone was used in this experiment. The main compositions include 97.3% of SiO_2 and 2.7% of $Al4[Si_4O_{10}](OH)_8$ without argillaceous water-soluble substances. According to the size of the testing system, rock specimens were processed to cylindrical specimens with a diameter of 75 mm and a height of 70 mm. They were divided into approximately equal two parts, forming a pair of rough fracture surfaces, which were parallel to each other, as shown in Figure 4. Then, circular holes with a diameter of 8 mm were processed in the middle of the fracture surface in any part and penetrated specimens along the height direction. Figure 2 shows the whole processing of rock mass specimens. 3D scanning system was applied to get structural characteristics of upper and lower fracture surfaces of specimens, as shown in Figure 5. The method in literature was used to calculate the roughness coefficient of the fracture surface, and $R_s = 1.38$, which was basically the same with that of the fracture surface of the natural rock [37, 38]. Specimens were fixed and installed to upper and lower bases of the seepage system, as shown in Figure 2 (13) and were sealed by sealing materials, as shown in Figure 2 (12). Thus, fractures with various openings were obtained by adjusting the distance between the upper and lower base.

The water-sediment mixture and quartz sands were adopted. Four groups of sands with different sand particle sizes ($d_s = 0.092 \sim 0.138$ mm, $0.138 \sim 0.184$ mm, $0.184 \sim 0.230$ mm, and $0.230 \sim 0.276$ mm) were used to prepare mixed solutions of various mass concentrations, as shown in Figure 6.

The concentration ρ_s of the mixture could be calculated by the following formula:

$$\rho_s = \frac{M_s}{B_\omega(1 + (M_s/m_s))}, \quad (13)$$

where the mass of the sand is M_s, the volume of water is B_ω, and the mass of water is m_s.

According to formula (13), the mass of the quartz sands with various concentrations could be obtained as follows

$$M_s = \frac{\rho_s B_\omega}{1 - \rho_s B_\omega / m_s}. \quad (14)$$

2.3. Experimental Scheme and Process

2.3.1. Experimental Methods and Process. Before the experiment, two specimens were fixed to the upper and lower bases by high water materials, respectively. Rock fractures with different openings were formed by adjusting the distance between the upper and lower bases. The water-sediment mixture was transported to the through hole to enter the fracture by the transport system. Figure 7 shows the radial direction of the mixture in fractures. The mixture flowing through the rock fractures ran back into the stirring pool through the return line.

With the diameter of the through hole of the lower specimen of $2a_2$, the specimen diameter of $2a_1$, the fracture width of b, the pressure at the inlet of the permeameter of P_0

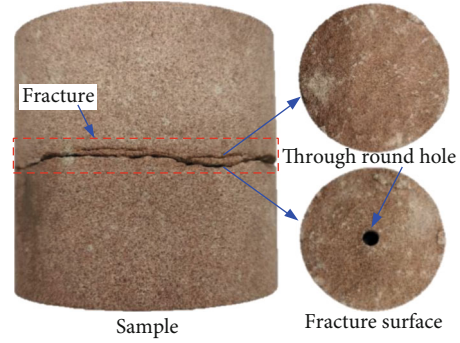

FIGURE 4: Rock specimens.

(approximately zero), the flow of Q, and the seepage velocity could be calculated as follows:

$$v(y)|_{y=r} = \frac{Q}{2\pi br}, \quad r \in [a_2, a_1]. \quad (15)$$

The average seepage velocity is as follows:

$$V = \frac{1}{\pi(a_1^2 - a_2^2)} \int_0^{2\pi} \int_{a2}^{a_1} \frac{Q}{2\pi br} r dr d\theta = \frac{Q}{\pi(a_1 + a_2)b}. \quad (16)$$

Supposing that there was no pressure loss in the through hole of lower specimen, the average value of the pressure gradient in fractures is as follows:

$$\overline{\frac{\partial p}{\partial x}} = -\frac{p_0}{a_1 - a_2}. \quad (17)$$

The absolute value is as follows:

$$G^p = \frac{p_0}{a_2 - a_1}. \quad (18)$$

During the experiment, the stable seepage flow Q_i and pressure P_i at the inlet of the permeameter under different rotational speeds were obtained by adjusting the motor speed n_i of the screw pump. According to formulas (16) and (17), the corresponding average seepage velocity V_i and pressure gradient G_i^p could be calculated, where i represented the level of the motor speed, that is, $i = 1, 2 \dots 11$.

Figure 8 shows the whole experimental process as follows.

2.3.2. Experimental Scheme. Table 1 shows 11 levels of the motor speeds of the single screw pump.

The motor speed was firstly step-by-step increased and then decreased. Then, hysteresis characteristics of the seepage process could be further judged and analyzed by calculating the average seepage velocity and pressure gradient during two stages. The seepage hysteresis can be judged and further analyzed according to equations (9) and (12).

This experiment mainly studied the influences of the sand particle size d_s, sand mass concentration ρ_s, and fracture

(a) Measurement method

(b) Upper fracture surface
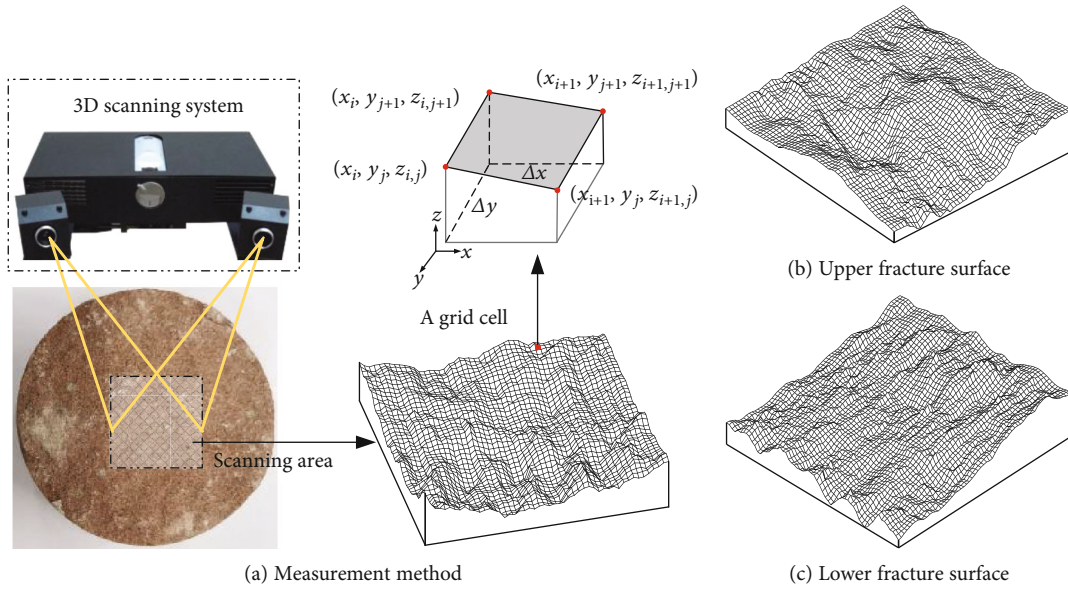
(c) Lower fracture surface

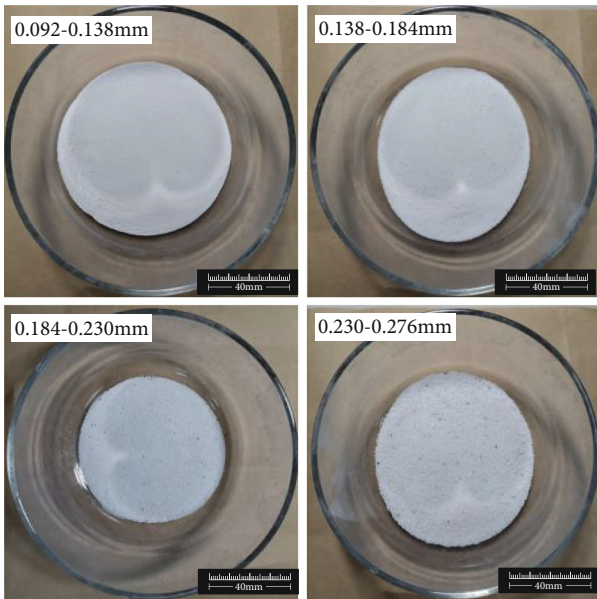FIGURE 5: Roughness test of rock specimen fracture surfaces.

FIGURE 6: Various SiO sand.

opening b on seepage hysteresis. Table 2 gives the specific parameters.

3. Determination of Hysteresis Characteristic Parameters of Water-Sediment Mixture Seepage

3.1. Judgement of Hysteresis Characteristics. Figures 9(a) and 9(b) show change curves of the seepage velocity and pressure gradient with time. The overall changes of curves were basically the same. Firstly, the seepage velocity and pressure gradient showed a ladder-shaped and gradual increase during the loading process. They increased rapidly and reached a
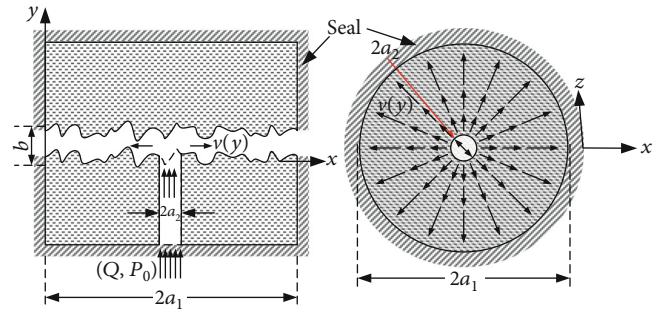

FIGURE 7: Radial direction of the mixture in fractures.

stable value in a relatively short period with the increase of the motor speed. The stable value was the average value. Secondly, the seepage velocity and pressure gradient showed a ladder-shaped and gradual decrease during the unloading process. They decreased rapidly and reached a stable value with the decrease of the motor speed.

By comparing Figures 9(a) and 9(b), it can also be found out that seepage velocities were the same during the two processes, and there were differences in pressure gradients. Both of them could meet formula (12), showing that obvious hysteresis characteristics exited in water-sediment mixture seepage in rock fractures in this experiment.

3.2. Hysteresis Parameters. On the basis of Figure 9, the pressure gradient and seepage velocity curves, namely, the hysteresis curves of the water-sediment mixture seepage, under steady-state could be obtained [39], as shown in Figure 10. The curves can be divided into the loading stage of $\overset{\frown}{OAB}$ and the unloading stage of $\overset{\frown}{BA^{*}O}$. In the former stage, the seepage velocity increased gradually, and then gradually decreased in the latter stage. The curves had common endpoints of O and B, between which there were no coincident
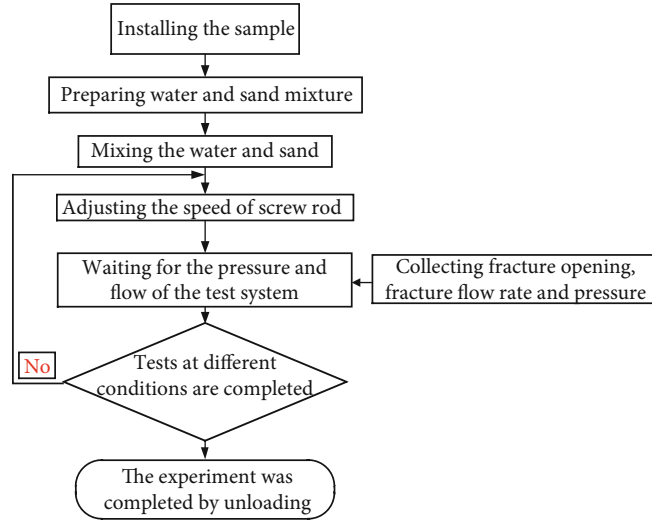
FIGURE 8: Experimental process of the seepage in rock fractures.

TABLE 1: Motor speeds.

ni (r/min-1)	$i = 1$	$i = 2$	$i = 3$	$i = 4$	$i = 5$	$i = 6$	$i = 7$	$i = 8$	$i = 9$	$i = 10$	$i = 11$
	200	400	600	800	1000	1200	1000	800	600	400	200

TABLE 2: Parameters.

Specimen no.	Fixed parameter	Variables
DS1—DS4	$b = 0.5$ mm, $\rho_s = 80$ kg/m^3	$d_s1 = 0.092 \sim 0.138$ mm; $d_s2 = 0.138 \sim 0.184$ mm $d_s3 = 0.184 \sim 0.230$ mm; $d_s4 = 0.230 \sim 0.276$ mm
RS1—RS4	$b = 0.5$ mm $d_s = 0.230 \sim 0.276$ mm	$\rho_s1 = 20$ kg/m^3; $\rho_s2 = 40$ kg/m^3 $\rho_s3 = 60$ kg/m^3; $\rho_s4 = 80$ kg/m^3
B1—B5	$d_s = 0.230 \sim 0.276$ mm $\rho_s = 80$ kg/m^3	$b1 = 0.5$ mm; $b2 = 0.5$ mm; $b3 = 0.5$ mm $b4 = 0.5$ mm; $b5 = 0.5$ mm

(a) Variation curve of seepage velocity
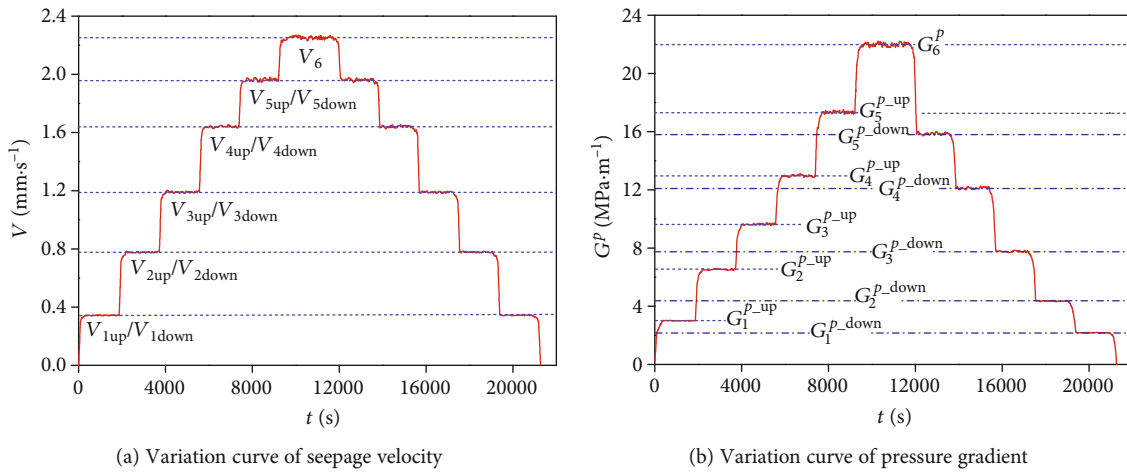

(b) Variation curve of pressure gradient

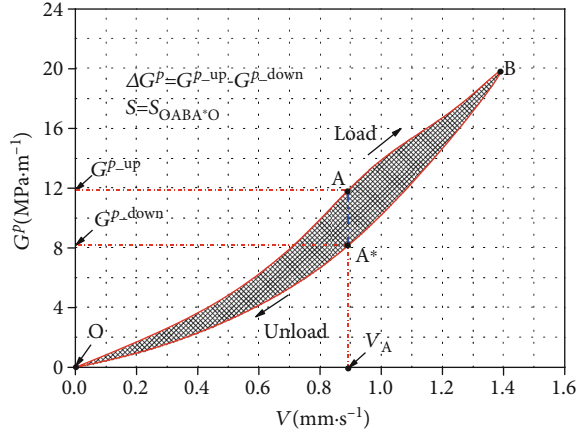FIGURE 9: Variation curve of seepage parameters with time.

Figure 10: Water-sediment mixture seepage hysteresis loop curves.

points. Meanwhile, the pressure gradient at the latter stage was always lower than that at the former stage under the same seepage velocity. The selection of hysteresis parameters mainly depended on the following two features:

(1) The degree of differences between the loading and unloading stage, that is, the area of the hysteresis S

(2) The largest degree of differences between the loading and unloading stage, that is, the maximum pressure gradient difference value ΔG_p under the same seepage velocity

Figure 10 gives the expressions and calculating methods of S and ΔG_p.

4. Hysteresis Characteristics of Water-Sediment Mixture Seepage in Fractures under the Influence of Different Factors

According to the experimental plan, the experiment on the influences of various sand particle size, sand mass concentration, and fracture opening on water-sediment mixture seepage in fractured rock specimens was carried out in order to get hysteresis characteristics.

4.1. Variation Laws of Water-Sediment Mixture Seepage Hysteresis Characteristics with Sand Particle Size. Figure 11 shows water-sediment mixture seepage hysteresis change curves with hysteresis characteristics parameters with the fixed fracture opening b of 0.5 mm, the sand mass concentration ρ_s of 80 kg·m³, and four groups of sand particle sizes. The shape of each hysteresis curve in Figure 11(a) was basically the same with that of the typical characteristic curve in Figure 10. A complete closed loop was formed without coincident points. The hysteresis curve characteristics indicated that the pressure gradient became larger with the increase of the sand particle size under the same seepage velocity during the loading stage. While the area of the whole hysteresis loop increased with the increasing descending speed of the curve during the unloading stage. In formula (17), the larger the pressure gradient, the larger the pressure

at the specimen inlet is. This was mainly because the larger particle volume had a bigger moment of inertia under the same motor speed, thus, making the large-volume mixture have larger initial pressure. The pressure loss of the mixture also became larger under inertia effects during the unloading stage, and the descending speed of the hysteresis curves became larger. In Figure 11(a), the variation curve of parameters with the sand particle size was obtained. d_s is the average of the sand particle size range, as shown in Figure 11(b). In Figure 11(b), the area of hysteresis S and the maximum pressure gradient difference ΔG_p under the same seepage velocity increased gradually as the particle size increased, approximately following an exponential change. When the sand particle size was relatively small, its increase had little influence on the hysteresis parameters. d_s increased from 0.092~0.138 to 0.138~0.184. S and ΔG_p increased by 14.29% from 0.980 to 1.120 and 45.40% from 0.544 to 0.791, respectively. As the sand particle size further increased, the hysteresis parameters showed a rapid and geometric increase. d_s increased from 0.138~0.184 to 0.230~0.276, and S increased by 3.82 times from 1.120 to 5.503. ΔG_p increased 3.74 times from 0.791 to 3.752. From the perspective of the seepage mechanics, when the sand particle size was relatively small, the water-sediment mixture was taken as the single seepage liquid. As the sand particle size increased, the effects of inertia became more significant. When the sand particle size increased to a certain extent, as part of the seepage channel, a two-phase flow pattern was formed, which was the main reason why S and ΔG_p increased gradually after the increase of sand particle size.

4.2. Variation Laws of Water-Sediment Mixture Seepage Hysteresis Characteristics with Sand Mass Concentration. Figure 12(a) shows hysteresis curves of water-sediment mixture seepage in fractured rock specimens with the fixed fracture opening b of 0.5 mm, sand particle size of 0.230~0.276 mm, and various sand mass concentrations. It could be observed that there were no intersections of curves both during the loading and unloading stages under various conditions. The start and end points coincided and formed a whole closed hysteresis. During the loading stage, the pressure gradient became larger as the mass concentration increased under the same seepage velocity, indicating that the initial pressure at the specimen inlet was larger. While the descending speed of the pressure gradient gradually increased as the mass concentration increased. Meanwhile, S increased with the increase of the mass concentration. The higher the sand mass concentration, the larger the mass of the mixture per unit volume. To reach the same seepage velocity, the initial seepage pressure under a high-concentration mixed solution would be higher. While the higher the concentration, the decrease of the seepage pressure in velocity and degree would be larger during the unloading stage. According to Figure 12(a), change curves of S and ΔG_p with the sand mass concentration could be obtained, as shown in Figure 12(b). The increase of sand mass concentration could effectively enhance hysteresis parameters, showing a linear type. With fixed sand particle
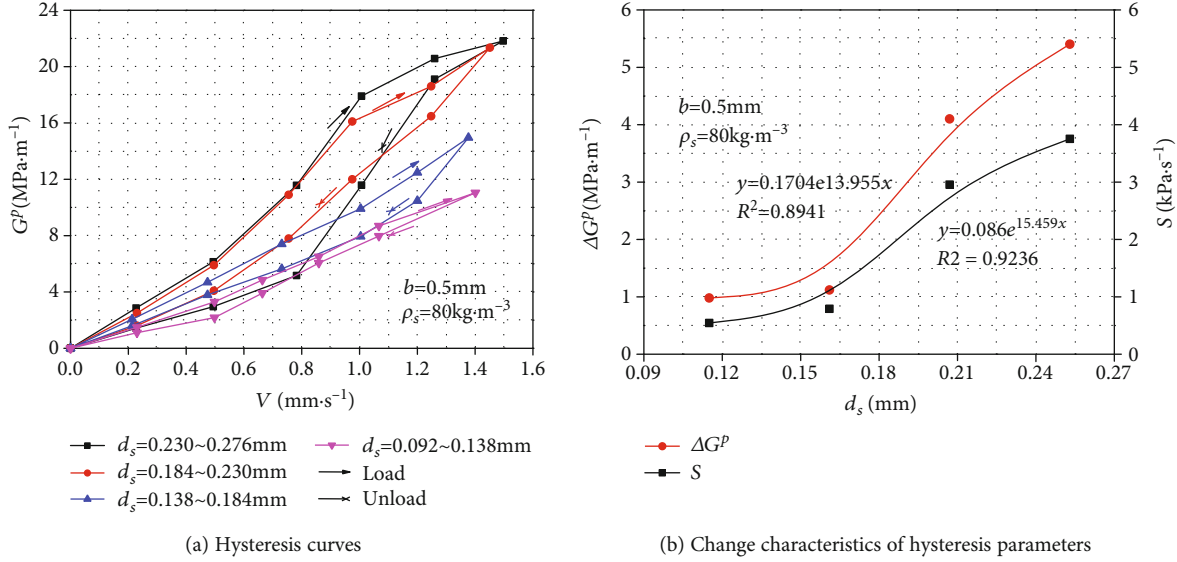
(a) Hysteresis curves

(b) Change characteristics of hysteresis parameters

FIGURE 11: Hysteresis characteristics of water-sediment mixture seepage in fractures under the effects of sand particle size.

(a) Hysteresis curves

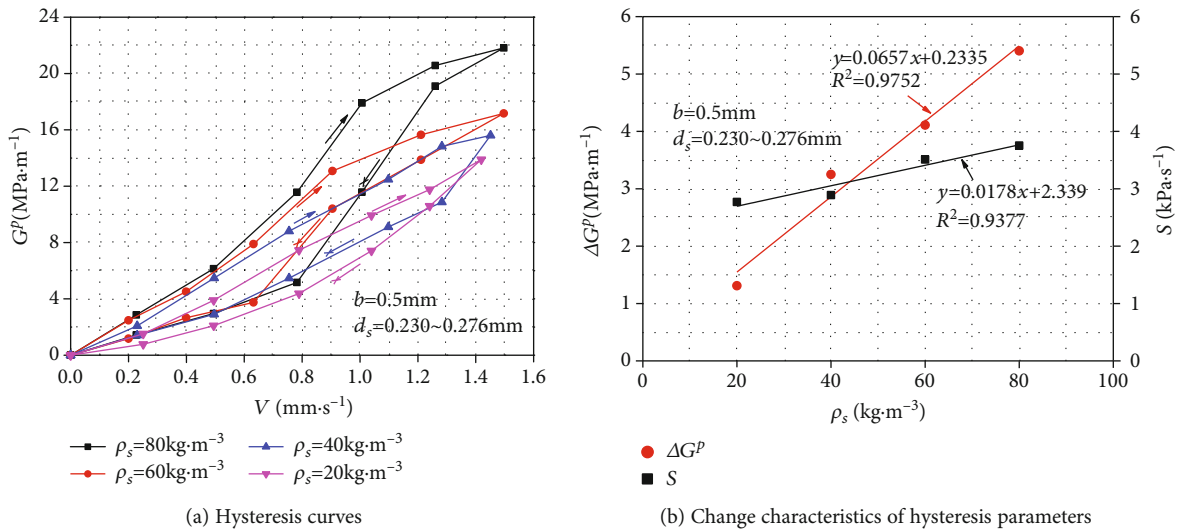(b) Change characteristics of hysteresis parameters

FIGURE 12: Hysteresis characteristics of water-flow seepage under the influence of sand mass concentration.

size and fracture opening, as the sand mass concentration increased, the seepage velocity and pressure gradient increased rapidly in linear type. The mass concentration increased from $20 \, \text{kg/m}^3$ to $80 \, \text{kg/m}^3$. S increased from 2.770 to 3.752, increasing by 3.12 times. ΔG_p increased from 2.770 to 3.752, increasing by 35.45%. The higher the sand mass concentration, the higher the mixed solution viscosity per unit volume and the larger the coefficient of viscosity. Thus, the differences between the loading and unloading stages of rock specimen fractures increased, reflecting that hysteresis parameters gradually increased.

4.3. Variation Laws of Water-Sediment Mixture Seepage Hysteresis with Fracture Opening. The fracture opening is another influence factor of hysteresis. Figure 13(a) shows

hysteresis curves under five groups of fracture opening. The sand mass concentration and sand particle size were fixed during the experiment ($\rho_s = 80 \, \text{kg} \cdot \text{m}^{-3}$ and $d_s = 0.230 \sim 0.276 \, \text{mm}$). It could be observed that there were no intersections of curves both during the loading and unloading stages. There were common starting and ending points. A complete hysteresis loop was formed. Fracture opening had different effects on the pressure gradient during the loading period, and the curves were basically coincident. While the change rate and S increased gradually during the unloading period. Figure 13(b) shows change curves of S and ΔG_p with the fracture opening. As the opening increased, S and ΔG_p gradually decreased in logarithmic form. The opening increased from 0.5 mm to 1.5 mm. S and ΔG_p decreased from 3.752 and 5.403 to 0.580 and 0.670, decreasing by 84.54% and 87.60%,

(a) Hysteresis curves
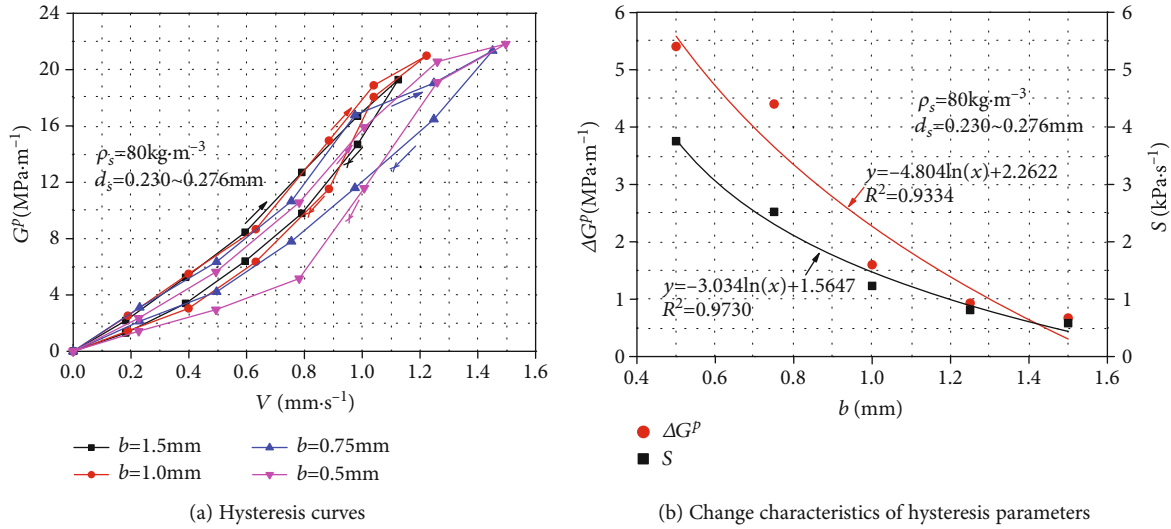
(b) Change characteristics of hysteresis parameters

FIGURE 13: Water-sediment mixture seepage hysteresis characteristics under the influence of fracture opening.

respectively. The more the openings, the less the friction effect of the fracture surface on the mixture, the closer to the ideal seepage characteristics, as shown in Figure 1. The seepage velocity was in the parabolic distribution along the normal direction along the fracture surface. The hysteresis characteristics of the seepage in rock fractures became weaker, thus, leading to smaller hysteresis parameters. It could be predicted that when the opening further increased, the influence of fracture surface on seepage characteristics of the mixture would be weakened.

5. Conclusions

In order to study the water-sediment mixture seepage hysteresis characteristics in rock fractures, theoretical analysis and seepage mechanics experiment were conducted. The influence factors of sand particle size, sand mass concentration, and fracture opening were studied in detail. The main conclusions are as follows.

According to the theory of seepage mechanics, a two-dimensional seepage mechanics model was first established. The relationships between the ideal seepage velocity and the pressure gradient were derived. On the basis, the methods of distinguishing water-sediment mixture seepage hysteresis characteristics in actual rock fractures were developed. The area of the hysteresis loop (S) and the maximum pressure gradient difference (ΔG_p) were selected as characterization parameters.

Second, a testing system was established to study the water-sediment mixture hysteresis characteristics in rock fractures. The corresponding testing process and methods were designed. The experiments were carried out under various conditions, and the hysteresis characteristics were judged and analyzed.

The experimental results indicated that with the increase of sand particle size, S and ΔG_p gradually increased exponentially, and the sensibility of the increase in hysteresis charac-

teristics also enhanced. S and ΔG_p rapidly increased with the increase of the sand mass concentration. While as the fracture opening increased, S and ΔG_p decreased in logarithmic form, indicating that when the opening reached a certain degree, hysteresis characteristics would not change anymore.

Data Availability

All data, models, and code generated or used during the study appear in the published article.

Conflicts of Interest

The authors declare that they have no conflict of interest to this work.

Acknowledgments

References

[1] W. J. Sun, W. F. Zhou, and J. Jiao, "Hydrogeological classification and water inrush accidents in China's coal mines," *Mine Water & the Environment*, vol. 35, no. 2, pp. 214–220, 2016.

[2] C. Zhu, X. X. Xu, W. R. Liu et al., "Softening Damage Analysis of Gypsum Rock With Water Immersion Time Based on Laboratory Experiment," *IEEE Access*, vol. 7, pp. 125575–125585, 2019.

[3] D. Ma, M. Rezania, H. S. Yu, and H. B. Bai, "Variations of hydraulic properties of granular sandstones during water inrush: effect of small particle migration," *Engineering Geology*, vol. 217, pp. 61–70, 2017.

[4] F. Wang, S. Tu, C. Zhang, Y. Zhang, and Q. Bai, "Evolution mechanism of water-flowing zones and control technology for longwall mining in shallow coal seams beneath gully topography," *Environmental Earth Sciences*, vol. 75, no. 19, pp. 1–16, 2016.

[5] B. Chen, S. Zhang, Y. Li, and J. Li, "Experimental study on water and sand inrush of mining cracks in loose layers with different clay contents," *Bulletin of Engineering Geology and the Environment*, vol. 80, pp. 663–678, 2020.

[6] K. Zhang, B. Zhang, J. Liu, D. Ma, and H. Bai, "Experiment on seepage property and sand inrush criterion for granular rock mass," *Geofluids*, vol. 2017, Article ID 9352618, 10 pages, 2017.

[7] D. K. Zhang, Z. L. Gu, R. X. Liang et al., "Impacts of Pore-Throat System on Fractal Characterization of Tight Sandstones," *Geofluids*, vol. 2020, Article ID 4941501, 17 pages, 2020.

[8] Y. X. Peng, L. Wu, Q. J. Zuo, C. H. Chen, and Y. Hao, "Risk assessment of water inrush in tunnel through water-rich fault based on AHP-Cloud model," *Geomatics, Natural Hazards and Risk*, vol. 11, no. 1, pp. 301–317, 2020.

[9] Y. L. Zhao, S. L. Luo, Y. X. Wang, W. J. Wang, L. Y. Zhang, and W. Wan, "Numerical analysis of karst water inrush and a criterion for establishing the width of water-resistant rock pillars," *Mine Water and the Environment*, vol. 36, no. 4, pp. 508–519, 2017.

[10] X. Zhang, H. Chen, C. Yao et al., "Seepage characteristics of triaxial compression-induced fractured rocks under varying confining pressures," *International Journal of Geomechanics*, vol. 20, no. 9, 2020.

[11] B. H. Guo, C. L. Wang, L. Wang, Y. Chen, and T. Cheng, "A modified cubic law for rough-walled marble fracture by embedding peak density," *Advances in Civil Engineering*, vol. 2020, Article ID 9198356, 10 pages, 2020.

[12] F. Ye, J. C. Duan, W. X. Fu, and X. Y. Yuan, "Permeability properties of jointed rock with periodic partially filled fractures," *Geofluids*, vol. 2019, 14 pages, 2019.

[13] T. L. Xiao, M. Huang, and M. Gao, "Triaxial permeability experimental study on deformation and failure processes of single-fractured rock specimens," *Shock and Vibration*, vol. 2020, Article ID 7329825, 12 pages, 2020.

[14] Y. D. Chen, W. G. Liang, H. J. Lian, J. F. Yang, and V. P. Nguyen, "Experimental study on the effect of fracture geometric characteristics on the permeability in deformable rough-walled fractures," *International Journal of Rock Mechanics and Mining Sciences*, vol. 98, pp. 121–140, 2017.

[15] H. Y. Pan, D. W. Yin, N. Jiang, and X. G. Xia, "Crack Initiation Behaviors of Granite Specimens Containing Crossing-Double-Flaws with Different Lengths under Uniaxial Loading," *Advances in Civil Engineering*, vol. 2020, Article ID 8871335, 13 pages, 2020.

[16] Z. M. Chao, G. T. Ma, X. W. Hu, and G. Luo, "Research on anisotropic permeability and porosity of columnar jointed rock masses during cyclic loading and unloading based on physical model experiments," *Bulletin of Engineering Geology and the Environment*, vol. 79, pp. 5433–5454, 2020.

[17] T. H. Yang, P. Jia, W. H. Shi, P. T. Wang, H. L. Liu, and Q. L. Yu, "Seepage-stress coupled analysis on anisotropic characteristics of the fractured rock mass around roadway," *Tunnelling and Underground Space Technology*, vol. 43, pp. 11–19, 2014.

[18] W. T. Xu, Y. S. Zhang, X. Z. Li, X. Y. Wang, and P. X. Zhang, "Study on three-dimensional fracture network connectivity path of rock mass and seepage characteristics based on equivalent pipe network," *Environmental Earth Sciences*, vol. 78, no. 16, article 516, 2019.

[19] S. H. Chen, X. M. Feng, and S. Isam, "Numerical estimation of REV and permeability tensor for fractured rock masses by composite element method," *International Journal for Numerical and Analytical Methods in Geomechanics*, vol. 32, no. 12, pp. 1459–1477, 2008.

[20] Q. X. Meng, H. L. Wang, M. Cai, W. Y. Xu, X. Y. Zhuang, and T. Rabczuk, "Three-dimensional mesoscale computational modeling of soil-rock mixtures with concave particles," *Engineering Geology*, vol. 277, article 105802, 2020.

[21] W. H. Tan and P. F. Wang, "Experimental study on seepage properties of jointed rock-like samples based on 3D printing techniques," *Advances in Civil Engineering*, vol. 2020, Article ID 9403968, 10 pages, 2020.

[22] F. Du, G. H. Jiang, and Z. Q. Chen, "A numerical simulation study of the migration law of water-sand two-phase flow in broken rock mass," *Geofluids*, vol. 2018, Article ID 6418476, 12 pages, 2018.

[23] Q. Liu and B. Liu, "Experiment study of the failure mechanism and evolution characteristics of water–sand inrush geo-hazards," *Applied sciences*, vol. 10, no. 10, article 3374, 2020.

[24] Y. Liu and S. C. Li, "Influence of particle size on non-Darcy seepage of water and sediment in fractured rock," *SpringerPlus*, vol. 5, no. 1, article 2099, 2016.

[25] Y. Zhang, M. Zhao, K. C. S. Kwok, and M. M. Liu, "Computational fluid dynamics-discrete element method analysis of the onset of scour around subsea pipelines," *Applied Mathematical Modelling*, vol. 39, no. 23-24, pp. 7611–7619, 2015.

[26] Z. Li, H. Zhou, D. W. Hu, and C. Q. Zhang, "Yield Criterion for Rocklike Geomaterials Based on Strain Energy and CMP Model," *International Journal of Geomechanics, vol.*, vol. 20, no. 3, 2020.

[27] W. F. Yang, L. Jin, and X. Q. Zhang, "Simulation test on mixed water and sand inrush disaster induced by mining under the thin bedrock," *Journal of Loss Prevention in the Process Industries*, vol. 57, pp. 1–6, 2019.

[28] Z. Li, S. Liu, W. Ren, J. Fang, Q. Zhu, and Z. Dun, "Multiscale laboratory study and numerical analysis of water-weakening effect on shale," *Advances in Materials Science and Engineering*, vol. 2020, Article ID 4020013, 2020.

[29] A. Sharma and B. Kumar, "Sheet flow hydrodynamics over a non-uniform sand bed channel," *International Journal of Sediment Research*, vol. 33, no. 3, pp. 313–326, 2018.

[30] Y. Q. Shi, C. Zhao, Z. Q. Peng, H. Y. Yang, and J. P. He, "Analysis of the lag effect of embankment dam seepage based on delayed mutual information," *Engineering Geology*, vol. 234, pp. 132–137, 2018.

[31] W. J. Xiao, D. M. Zhang, and X. J. Wang, "Experimental study on progressive failure process and permeability characteristics of red sandstone under seepage pressure," *Engineering Geology*, vol. 265, article 105406, 2020.

[32] Z. Bednarczyk, "Identification of *flysch* landslide triggers using conventional and 'nearly real-time' monitoring methods - an example from the Carpathian Mountains, Poland," *Engineering Geology*, vol. 244, pp. 41–56, 2018.

[33] C. X. Huang, X. H. Wang, M. Zhang, H. Zhou, and Y. Liang, "Supporting characteristics of soldier piles for foundation pits under rainfall infiltration," *Advances in Civil Engineering*, vol. 2019, Article ID 1053576, 10 pages, 2019.

[34] K. Liao, Y. Wu, F. Miao, L. Li, and Y. Xue, "Time-varying reliability analysis of Majiagou landslide based on weakening of hydro-fluctuation belt under wetting-drying cycles," *Landslides*, vol. 18, pp. 267–280, 2021.

[35] X. F. Wang, C. G. Liu, S. J. Chen, L. Chen, K. Li, and N. Liu, "Impact of coal sector's de-capacity policy on coal price," *Rock Mechanics and Rock Engineering*, vol. 265, article 114802, 2020.

[36] C. Zhu, M. C. He, M. Karakus, X. B. Cui, and Z. G. Tao, "Investigating toppling failure mechanism of anti-dip layered slope due to excavation by physical modelling," *Rock Mechanics and Rock Engineering*, vol. 53, pp. 5029–5050, 2020.

[37] Y. Chen, G. Lin, R. Mao, M. Li, X. Mao, and K. Zhang, "Strain rate effect on the mechanical properties and fracture surface roughness of sandstone subjected to dynamic direct tension," *IEEE Access*, vol. 8, pp. 107977–107992, 2020.

[38] Q. Yin, R. I. Liu, H. W. Jing, H. J. Su, L. Y. Yu, and L. X. He, "Experimental study of nonlinear flow behaviors through fractured rock samples after high-temperature exposure," *Rock Mechanics and Rock Engineering*, vol. 52, no. 9, pp. 2963–2983, 2019.

[39] Z. Li, H. X. Liu, Z. L. Dun, L. W. Ren, and J. Fang, "Grouting effect on rock fracture using shear and seepage assessment," *Construction and Building Materials*, vol. 242, article 118131, 2020.